Journal of Fluids and Structures 17 (2003) 461–477

JOURNAL OF FLUIDS AND STRUCTURES

www.elsevier.nl/locate/jnlabr/yjfls

Characteristics of F/A-18 vertical tail buffeting

E.F. Sheta[a,*], L.J. Huttsell[b]

[a] *CFD Research Corporation, 215 Wynn Drive, Huntsville, AL 35805, USA*
[b] *AFRL, Wright-Patterson AFB, Dayton, OH 45433, USA*

Received 9 July 2001; accepted 16 September 2002

Abstract

A time-accurate computational analysis of vertical tail buffeting of full F/A-18 aircraft is conducted at typical flight conditions to identify the buffet characteristics of fighter aircraft. The F/A-18 aircraft is pitched at wide range of high angles of attack at Mach number of 0.243 and Reynolds number of 11 millions. Strong coupling between the fluid and structure is considered in this investigation. Strong coupling occurs when the inertial effect of the motion of the vertical tail is fed back into the flow field. The aerodynamic flow field around the F/A-18 aircraft is computed using the Reynolds-averaged full Navier–Stokes equations. The dynamical structural response of the vertical tail is predicted using direct finite-element analysis. The interface between the fluid and structure is applied using conservative and consistent interfacing methodology. The motion of the computational grid due to the deflection of the vertical tail is computed using transfinite interpolation module. The investigation revealed that the vertical tail is subject to bending and torsional responses, mainly in the first modes of vibrations. The buffet loads increase significantly as the onset of vortex breakdown moves upstream of the vertical tails. The inboard surface of the vertical tail has more significant contribution in the buffet excitation than the outboard surface. In addition, the pressure on the outboard surface of the vertical tail is less sensitive to the angle of attack than the pressure on the inboard surface. The buffet excitation peaks shift to lower frequency as the angle of attack increases. The computational results are compared, and they are in close agreement, with several flight and experimental data.
Published by Elsevier Science Ltd.

1. Introduction

Fighter aircraft have been designed to fly and maneuver at high angles of attack and at high loading conditions. At these high angles of attack, the flow separates from the sharp leading edges of the wing and leading-edge extension (LEX) forming a strong vortical flow that maintains the stability of the aircraft. However, the leading-edge vortices break down upstream of the vertical tails. The breakdown flow impinges upon the vertical tail surfaces causing severe structural fatigue and has lead to their premature fatigue failure, costing millions of dollars every year for inspections and repairs. The accurate prediction and analysis of the tail buffet problem remains a prime objective to improve the design and maneuverability of the new generation of fighter aircraft.

Extensive experimental research work has been conducted to identify the characteristics of the buffet problem. The F/A-18 aircraft, in particular, was the subject of numerous research work, see Wentz (1987), Sellers III et al. (1988), Lee and Brown (1990), and Moses and Pendleton (1996). These experiments showed that the vortical flow breaks down ahead of the vertical tail at angles of attack of 25° and higher. The breakdown flow produced unsteady and unbalanced loads on the vertical tails. At high angles of attack, the buffet pressure concentrates in a narrow, low-frequency band. Cole et al. (1990) measured vertical tail buffet responses of a 16% model of an F-18 aircraft over the range of angles of

*Corresponding author. Tel.: +1-256-726-4869; fax: +1-256-726-4806.
E-mail address: efs@cfdrc.com (E.F. Sheta).

0889-9746/03/$ - see front matter Published by Elsevier Science Ltd.
PII: S0889-9746(02)00138-X

Nomenclature

A_t	reference area of vertical tail, 4.842 m^2.
$\bar{C}$	mean aerodynamic chord of the wing, 3.5 m.
C_P	coefficient of pressure, $(P - P_\infty)/q_\infty$
$\bar{C}_P$	mean pressure coefficient, $\left[(1/N)\sum_1^N C_P\right]$
$\hat{C}_P$	r.m.s. pressure coefficient, $\left[(1/N)\sum_1^N (C_P - \bar{C}_P)^2\right]^{1/2}$
C_{rbm}	root bending moment coefficient, $M_B/q_\infty A_t \bar{C}$
$F(n)$	dimensionless buffet pressure power spectral density
FS	fuselage station
f	frequency (Hz)
M	Mach number
M_B	vertical tail root bending moment
N	number of sample points
n	nondimensional frequency, $f\bar{C}/U_\infty$
P_i	pressure on inboard tail surface
P_o	pressure on outboard tail surface
ΔP	differential pressure, $P_i - P_o$
q_∞	freestream dynamic pressure
Re	Reynolds number, $U_\infty \bar{C}/v$
U_∞	freestream velocity
α	angle of attack
v	freestream kinematic viscosity

attack from -10° to 40° and over the range of Mach numbers from 0.3 to 0.95. Their results indicated that the buffet response occurs mainly in the first bending mode, increases with increasing dynamic pressure and is larger at $M = 0.3$ than at higher Mach numbers. Bean and Lee (1994) conducted a wind-tunnel tests on a rigid 6% model of F/A-18 aircraft over a wide range of angles of attack up to 38°. They found that buffeting in the torsional mode occurred, at lower angles of attack, with larger amplitudes compared to those of the fundamental bending mode. Moses and Huttsell (2000) have shown that buffet characteristics of an early F-22 aircraft model are similar to what have been seen on the F/A-18 aircraft.

The buffeting of F/A-18 vertical tail was temporarily reduced using streamwise fences. The fences were fitted over the upper surface of the wing LEX near the leading edge of the wing, see Lee et al. (1990) and Shah (1991). The fence, although developed through trial and error wind-tunnel experiments, reduces the buffet loads experienced by the vertical tails. In flight tests by Lee and Valerio (1994), the acceleration peaks at a point close to the tip of the vertical tail were reduced from 450 g to 200 g with the addition of the LEX fence. A loss of 2 to 3% of maximum lift was seen, since the fence disrupts the basic vortical flow. The fences were also less effective at high angles of attack; see Shah (1991) and Meyn and James (1993). As part of the Actively Controlled Response of Buffet-Affected Tails program, Moses (1997) conducted wind-tunnel experiments on 1/6-scale F18 model. The starboard vertical tail was equipped with active rudder and the port tail was equipped with piezoelectric actuators. Power spectral densities of the root bending moment (rbm) at the frequency of the first bending mode were reduced by up to 60%.

Computationally, there have been limited attempts to analyze the buffet problem successfully. Rizk et al. (1992a, b) solved the Reynolds-averaged, thin-layer Navier–Stokes equations around the F/A-18 aircraft at $\alpha = 30^\circ$. A Chimera embedded grid consisting of 0.9 million cells was used to model the symmetric half of the aircraft. The aerodynamic results were qualitatively similar to some experimental data. Later, Gee et al. (1995) used 1.7 million cells to capture more robust vortices. A weak coupling between the aerodynamics and structures was considered by assuming rigid tails. Thus, the inertial effects of the acceleration of the tail points on the flow field were neglected. It is particularly noteworthy that Sheta et al. (2001) have shown that the inertial effects of the tail motion affect the vortex breakdown flow upstream of the vertical tails and affect the buffet loads upon the vertical tails. Gee et al. (1995) concluded that the dominant frequency is very close to the first natural frequency of the tail. The time history shows a pattern of near periodic fluctuations of the loads. Kandil et al. (1996, 1997) analyzed the twin-tail buffet of delta-wing/twin-tail model over wide range of angles of attack and spanwise locations of the tails. The results showed that the tail motion altered the vortex breakdown location and altered the unsteady buffet loads on the tails. The loads, deflections, and rbm were reduced as the twin tails moved laterally toward the vortex core. Sheta and Kandil (1998, 1999) studied the effects of

pitching motion and rolling oscillations on the twin-tail buffet responses. The buffet loads and responses were shown to increase when the breakdown location moved upstream crossing the wing trailing edge. Increasing the reduced frequency of rolling has led to higher loads and excitation peaks. However, the bending and torsion deflections were reduced. Sheta (2000) studied the effects of streamwise fences with several taper ratios on twin-tail buffet responses of generic fighter aircraft. The fence reduces the buffet loads and responses of the tails. However, the effectiveness of the fences reduced at very high angles of attack. The fences of taper ratio of 0.7 produced the most favorable results with minimal effect on the aerodynamics.

In this investigation, time-accurate high-fidelity computational analysis of vertical tail buffeting of full F/A-18 aircraft at typical flight conditions is presented. The objective of the study was to identify the characteristics of vertical tail buffeting of fighter aircraft at high angles of attack, and to study the effect of angle of attack on the buffet excitation and frequency. The results of this investigation are compared with several experimental and flight-test data.

2. Multidisciplinary technical approach

The tail buffet problem is a complex multidisciplinary aeroelastic phenomenon that involves interaction between several physical and numerical disciplines. The physical disciplines are the fluid dynamics of the flow field and the structure dynamics of the flexible surfaces. The numerical disciplines are the grid deformation and the fluid-structure interface coupling. In this investigation, the interface coupling between the fluid and structure is applied in a manner that ensures conservation of forces, moments, and virtual work. In order to ensure synchronization of data transfer between the different modules, the multidisciplinary modules are integrated into the multidisciplinary computing environment (MDICE). MDICE enables the engineering analysis modules to run concurrently and cooperatively on a distributed network of computers to perform multidisciplinary task. Next, the particular sets of analysis modules used in the current investigation are outlined.

2.1. Fluid-dynamics module

The buffet problem of vertical tails occurs at high angles of attack where the flow field is characterized by strong vortical flow and massive three-dimensional flow separation. In this case, the problem mandates the solution of the full Navier–Stokes equations to account for vorticity evolution, convection, shedding, vortex breakdown, and strong fluid–structure interactions. Euler and thin-layer Navier–Stokes equations can give an approximate solution in the region of primary vortices, but they cannot model the three-dimensional viscous effects or predict the accurate location and strength of the secondary and tertiary vortices.

In this investigation, the fluid-dynamics module CFD-FASTRAN (Hall, 1999) is used. The fluid-dynamics module solves the Reynolds-averaged full Navier–Stokes equations using an implicit finite volume upwind scheme with Roe's flux-difference splitting for spatial differencing and a fully implicit upwind scheme for temporal differencing.

The physical boundary conditions assume Riemann's inflow-outflow farfield boundary conditions. On the aircraft surfaces, the no-slip and no-penetration conditions are enforced, that is the relative velocity equals to zero. The normal pressure gradient equals to zero on stationary surfaces. On the accelerating tail surfaces, the normal pressure gradient is no longer zero due to the inertia of the moving tail. The pressure gradient on the accelerating surfaces becomes $\partial p/\partial \hat{n} = -\rho(\bar{a} \cdot \hat{n})$, where $\bar{a}$ is the acceleration of a point on the accelerating surface and $\hat{n}$ is the unit normal. This relation can be derived directly from the normal momentum equation. The temperature is enforced at the solid surfaces using adiabatic boundary conditions. At the grid interface boundaries, the solution is interpolated across the boundaries using conservative interpolation. Conservative interpolation seeks to conserve the forces and moments between two adjacent cells. Because of the symmetry of the F/A-18 aircraft, only half the aircraft is considered and symmetry boundary condition is assumed at the symmetry boundary.

2.2. Structural-dynamics module

The structural-dynamics response of the vertical tail is analyzed using direct finite-element analysis. The aeroelastic equations of motion of the vertical tail under the influence of the vortex breakdown flow are given by

$$[M]\{\ddot{Y}\} + [C]\{\dot{Y}\} + [K]\{Y\} = \{F\}, \tag{1}$$

where $\{Y\}$ is the displacement vector, $[M]$ is the mass matrix, $[C]$ is the damping matrix, $[K]$ is the stiffness matrix, and $\{F\}$ is the force vector due to the aerodynamic loads and shear stresses. The equations of motion of the vertical tails are solved using the finite-element stress code FEM-STRESS (Yang and Wang, 1994). The vertical tail of the F/A-18

aircraft is modelled using second-order quad shell elements. The shell elements have five degrees of freedom per structural node. These are the three Cartesian displacements plus two in-plane rotational motions. The module uses the degenerated shell-type element with eight nodal points to discretize the structure system. This element geometry is interpolated using the midsurface nodal point and midsurface nodal point normal. It is assumed that lines that are originally normal to the midsurface of the shell remain straight during the element deformation and that no transverse normal stress is developed.

2.3. Fluid–structure interfacing module

The fluid–structure interface algorithm is used to project the forces and moments from the fluid flow to the flexible-body structure and to feed back the aeroelastic deflections of the structure to the flow field. The interfacing is formulated in the most general sense for maximum flexibility. There are no inherent assumptions that the fluids grid is matched with the structure grid, either through different mesh densities, mesh architecture, or through physical separation between the interfaces, as seen with thick-shell finite-element models. The current simulation uses a conservative and consistent interface, adapted from Brown (1997). Conservative interfaces aim to conserve the forces and moments in the interpolation process between two grids. In this case, the sum of all forces and moments on the fluid interface is equivalent to the sum of all forces and moments on the structure interface. Consistency, or virtual work conservation, requires that the virtual work performed by the solid interface is equivalent to the virtual work performed by the fluid interface.

2.4. Grid deformation module

The inertial effect of the motion of the flexible tail is fed into the flow field through the boundary conditions at the solid interface, and through deformation of the flow field grid. The CFD grid is deformed at every fluid–structure data exchange to accommodate the deformed shape of the tail. The six outer boundary surfaces of the deformed grid block are kept fixed. The grid is deformed using the transfinite interpolation functions (TFI). The advantages of using TFI are that TFI is an interpolation procedure that deforms grids conforming to specified boundaries and it is very computationally efficient. The spacing between points in the physical domain is controlled by blending functions that specify how far into the original grid the effect of the new position of the flexible-body surfaces is carried. The grid points near the surface of the tails are moving with the deflections of the tail. The deformation of the grid points decreases as you go far from the boundary in all directions, and vanishes at the outer boundary of the deformed block. The TFI routine is invoked automatically when a fluid–structure interface is exchanged between application modules.

2.5. Multidisciplinary computing

The multidisciplinary modules used in the current investigation are integrated into the MDICE (Kingsley et al., 1998). MDICE is a distributed object-oriented environment for parallel execution of multidisciplinary modules. There are many advantages to the MDICE approach. Using MDICE environment, one can avoid giant monolithic codes that attempt to provide all modules in a single large computer program. Such large programs are difficult to develop and maintain and by their nature cannot contain up-to-date technology. MDICE allows the reuse of existing, state-of-the-art codes that have been validated. The flexibility of exchanging one application program for another enables each engineer to select and apply the technology best suited to the task at hand. Efficiency is achieved by utilizing a parallel-distributed network of computers. Extensibility is provided by allowing additional engineering programs and disciplines to be added, without modifying or breaking the modules or disciplines already in the environment.

3. Geometry modelling

The geometry of the full F/A-18 aircraft is modeled using a structured body-fitted grid system with one-to-one grid connectivity. The surface grid of the F/A-18 aircraft is shown in Fig. 1. The surface grid consists of the forebody, LEX, wing, vertical and horizontal tails, engine diffuser, inlet boundary layer diverter plate, exit vent, and pylon. The LEX fences are not modeled. The vertical tail rudder and the leading-edge flaps of the wing and horizontal tail are all set at zero angles. The full F/A-18 aircraft has an overall length of 17.1 m, a wingspan of 11.4 m, a wing reference area of 37.15 m^2, a wing mean aerodynamic chord of 3.51 m, and a vertical tail reference area of 4.842 m^2. The vertical tail has an aspect ratio of 1.2, a taper ratio of 0.4, and a leading-edge sweep angle of 41.4°. The vertical tail has a cantilever angle of 20° toward the outboard direction.

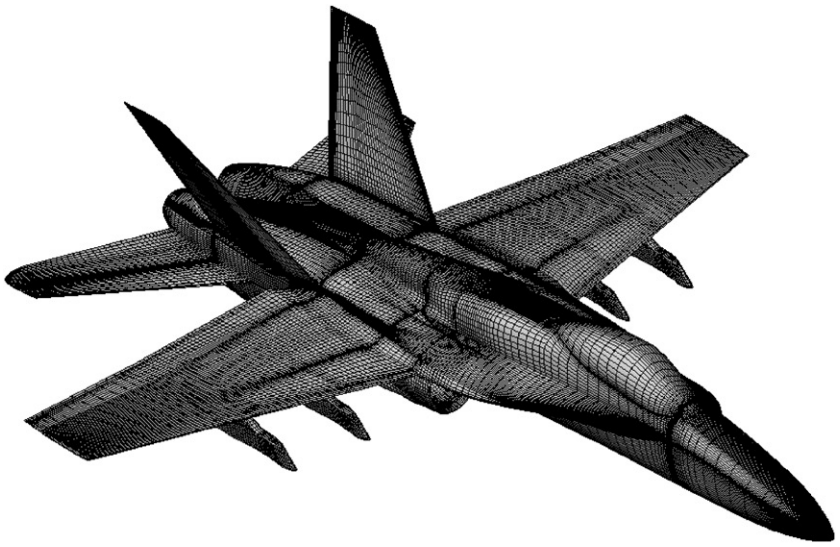

Fig. 1. Surface grid of the F/A-18 aircraft.

The grid is a multiblock H–H grid consisting of 53 structured blocks utilizing 2.56 million cells (2.68 million grid points). The global grid extends five wing chords upstream and downstream of the aircraft, and eight wing chords normal to the aircraft. The grid is clustered near the apex and leading edge of the wing LEX in order to produce robust and well-defined leading-edge vortices. The grid blocks are connected through the boundaries using one-to-one grid connectivity. No Chimera, overlapping or high-order grid connectivity methods were used. The grid topology on a cross-plane just ahead of the vertical tails is shown in Fig. 2. The grid around the vertical tail enables moving the grid points due to tail motion without regard to any grid discontinuity. If a Chimera grid were used, an extensive cutting of holes in the grid would be necessary for every iterations due to the motion of the tail.

For the structural-dynamics analysis, the vertical tail of the F/A-18 aircraft is modelled using second-order shell elements. The CFD and CSD surface grids of the vertical tail are shown in Fig. 3. The CFD and CSD grids are not identical and the forces and deflections are interpolated between the two grids using the conservative/consistent interfacing module outlined in the previous section. A total of 1840 grid cells defined the CFD surface grid of the tail, while 576 grid cells defined the CSD surface grid of the tail. The material of the vertical tail is assumed to be aluminum and isotropic. The Young's modulus of elasticity is $6.896 \times 10^{10}\,\mathrm{N/m^2}$, the density is $2765\,\mathrm{kg/m^3}$, and the Poisson's ratio is 0.33. The natural frequencies of the vertical tail are 15.5, 45 and 61 Hz for the first bending mode, first torsion mode, and second bending mode, respectively.

4. Results and discussion

The aerodynamic and aeroelastic fields around the full F/A-18 aircraft are analyzed at typical flight conditions. The flight conditions correspond to the NASA F/A-18 High Alpha Research Vehicle (HARV). The aircraft is pitched over wide range of angles of attack ($\alpha = 25^\circ - 40^\circ$) at $M = 0.243$ and $\mathscr{R}e = 11$ millions. The inlet mass flow rate of the engine is 63 ibm/s per engine, which corresponds to the maximum power condition. Strong coupling between the fluid and structure is considered in this investigation. Strong coupling occurs when the inertial effect of the motion of the solid is fed back into the fluid.

This multidisciplinary aeroelastic problem is solved using two steps: the first step solves for the vortical flow characteristics around the rigid configuration. The initial condition of this step is the undistributed free-stream condition. The solution is carried out for about 1500 time-accurate steps until the changes in the vortical flow field become insignificant. The second step solves for the aerodynamic flow field and aeroelastic responses of the flexible configuration. The initial condition of this step is the final solution of the first step. The time steps of the computations are fixed in all cases at 10^{-4} s.

The problem is solved on a Linux computer cluster of four units. The total grid is divided evenly between the four processors using domain decomposition. The speed of each processor is 1.0 GHz. Every partition of the grid requires

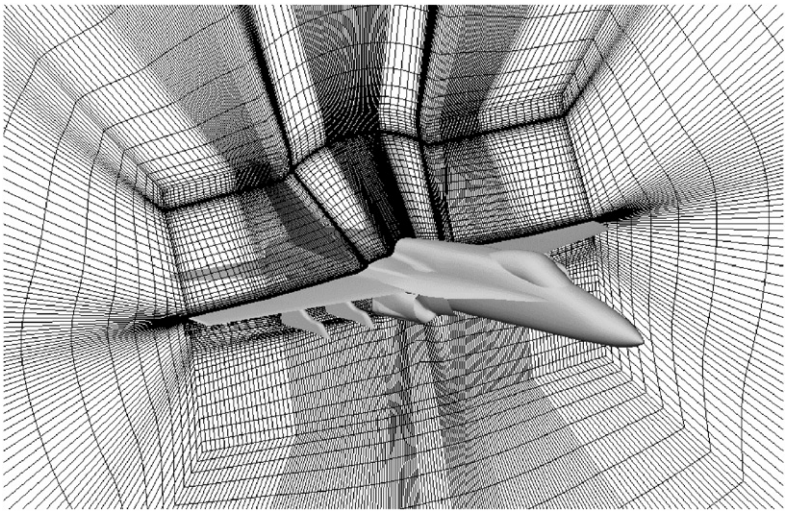

Fig. 2. The grid topology on cross-flow plane.

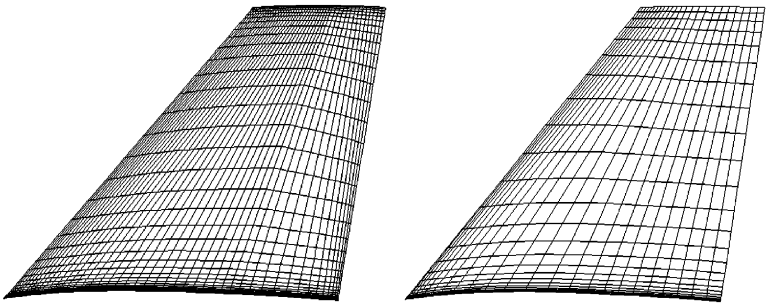

(a) (b)

Fig. 3. Surface CFD grid and CSD grid of the vertical tail: (a) CFD grid; (b) CSD grid.

approximately 200 MB of memory. For the current grid system, the problem requires about 57 μs per time step per grid point on the four unit cluster. Each case presented herein requires about 200 CPU working hours. When the same problem runs on one processor only, the total computational cost was about 768 CPU working hours. Therefore, about 4% of the total computational time was used for the data transfer between the four processors.

4.1. F/A-18 flow field characteristics

The total pressure contours on cross-flow planes at different longitudinal locations on the F/A-18 aircraft at 30° angle of attack are shown in Fig. 4. The oncoming flow initially attaches to the lower surface of the LEX then moves toward the leading edge. The flow separates from the sharp leading edge of the LEX forming a free-shear layer. The spanwise pressure gradient on the upper surface of the LEX cause the shear layer to move inward and rolls up into a concentrated spiral flow to form the primary vortex. The flow moving around the vortex is swept downward and reattaches on the upper surface of the LEX. The attached flow then moves outward underneath the primary vortex toward the leading edge. The pressure gradient induced by the primary vortex causes the attached flow to separate, forming a smaller secondary vortex that is rotated in the opposite direction to that of the primary vortex. As the flow travels downstream, the primary vortices gain strength and move upward and to the outward direction. As the flow moves downstream the wing apex, another vortex starts to roll up in the same way as the LEX vortex. This is the primary vortex of the wing. The figure shows that the vortical flow surrounding the LEX and the wing vortex cores merge together before they reach the vertical tail. The two vortices are trailing downstream and the vortex cores start to vanish; an indication of loss in the total pressure and axial momentum. Later, the vortex cores break down before they reach to the vertical tail.

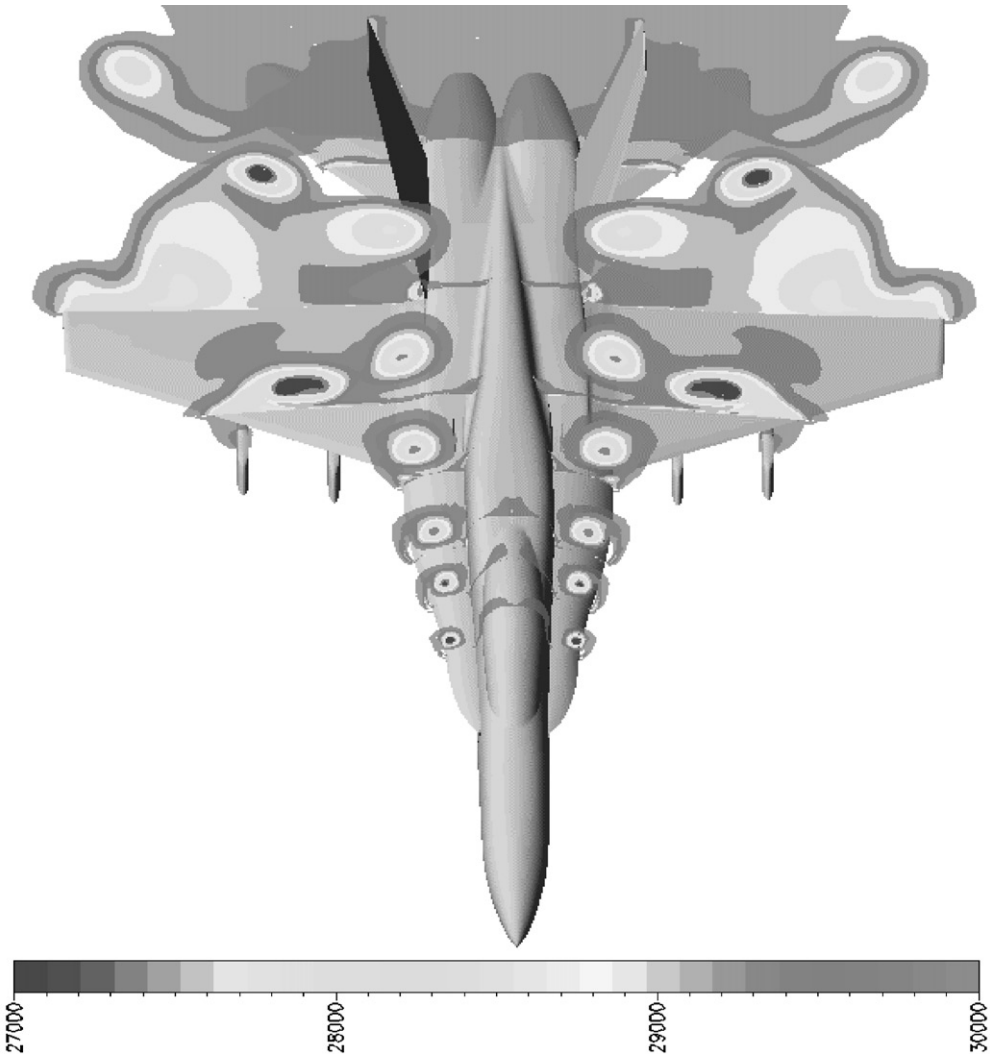

Fig. 4. Total pressure contours on cross-flow planes at different longitudinal stations.

Another vortex is generated at the tip of the wing that trails downstream away from the vertical tail. As the vortical flow crosses the leading edge of the vertical tail, a smaller vortex develops at the root of the tail underneath the primary LEX vortex. The tail vortex exists totally at the outer surface of the vertical tail and it is rotating in the opposite direction to that of the primary LEX vortex.

The surface pressure coefficient on the upper and lower surfaces of the LEX at different fuselage stations (FS) at $\alpha = 30^\circ$ are shown in Fig. 5. The results are compared with HARV flight-test data (Fisher et al., 1990) at three different FS. The spanwise coordinate is normalized by the span of the LEX at every FS, such that the normalized coordinate is zero at the leading edge of the LEX and one at the intersection with the fuselage. Two suction peaks are shown in the pressure distribution. The suction peaks correspond to the core of the primary and secondary LEX vortices, respectively. The pressure peaks and the positions of the vortex core of the primary vortex are accurately captured at all stations. However, the pressure peak of the secondary vortex at the aft position is overestimated. The figure shows the outboard motion of the core of the leading-edge vortices as the flow travels downstream. This is indicated form the outboard spanwise motion of the primary suction peak.

Three-dimensional and front view snapshots of the F/A-18 aircraft and the instantaneous streamlines of the LEX and wing vortices at four different angles of attack are shown in Fig. 6. The figure also shows the surface static pressure on the aircraft surfaces. The flow field at these high angles of attack is characterized by highly unsteady spiral flow, massive

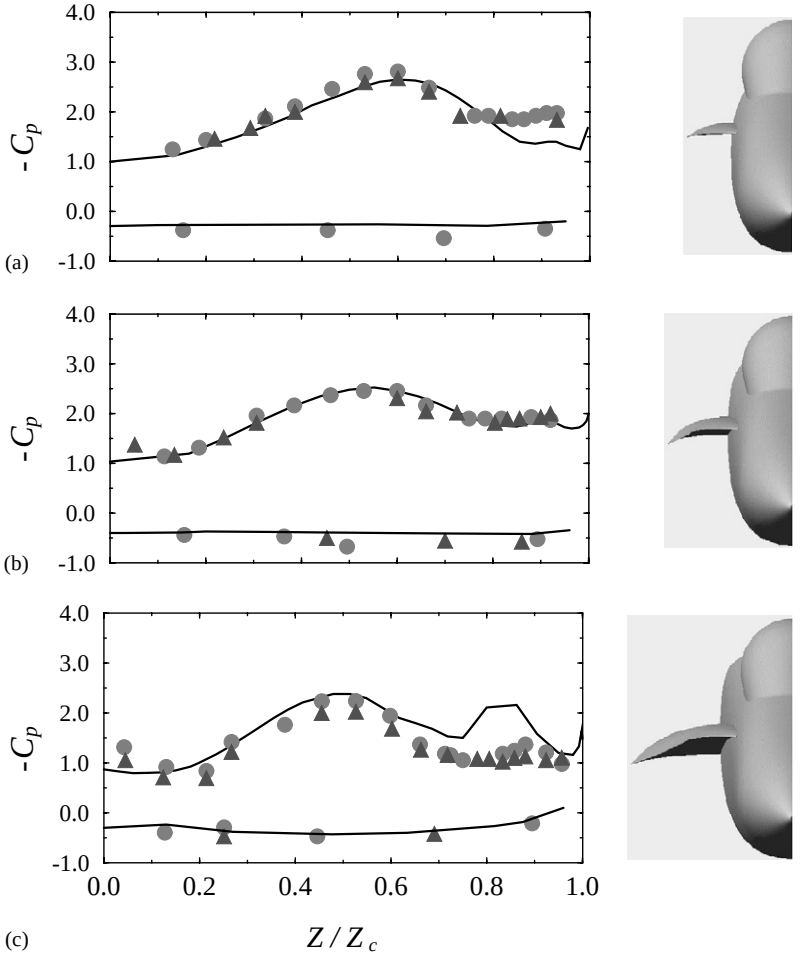

Fig. 5. Surface pressure coefficient over the LEX, compared with flight data of Fisher et al. (1990): (a) FS 253; (b) FS 296; (c) FS 357. ——, Present computation; ●, flight data (starboard); ▲, flight data (port).

three-dimensional separation, and unsteady vortex breakdown location. This obviously would impose different levels of pressure gradients upon the vertical tails. As the leading-edge vortex travels downstream, the core of the vortex makes an abrupt kink and forms a spiral vortex. The spiral vortex was also observed by Fisher et al. (1990) in flight tests of the F-18 HARV vehicle. The spiral vortex persists for several turns (especially at lower angles of attack) before breaking up. The sense of the spiral vortex is opposite to the direction of rotation of the leading-edge vortex. The sense of spiral vortex may have to be opposite to the direction of rotation of the main vortex in order to generate stagnant vortex core, a phenomenon that accompanies vortex breakdown; see Jumper et al. (1993). At an angle of attack of 25°, the LEX and wing vortices break down just ahead of the vertical tail. As the angle of attack increases, the onset of vortex breakdown moves upstream and upward, and the vortex breakdown flow becomes larger in size. The vertical tail emerges in the vortex breakdown flow at all angles of attack. The figure also shows that at higher angles of attack, the inboard space between the vertical tails entrains more vortical flow. The contour plots over the vertical tail shows that pressure gradient develops on the surfaces of the tail. The pressure gradient increases with the increase of angle of attack. In the cases considered herein, the flaps angles of the wing are considered zero. If the flaps of the wings are set at non-zero angles, the interaction between the LEX and wing vortices will be modified which may modify the buffet loads on the vertical tails.

The total pressure contours in a cross-flow plane at the leading edge of the wing root ($x = 9.5$ m) are shown in Fig. 7. Two vortices are shown in the figure. The inboard vortex corresponds to the LEX vortex. The outboard vortex corresponds to the wing vortex. At $\alpha = 25°$ and 30°, the core of the LEX vortex can be easily seen. At $\alpha = 35°$, the

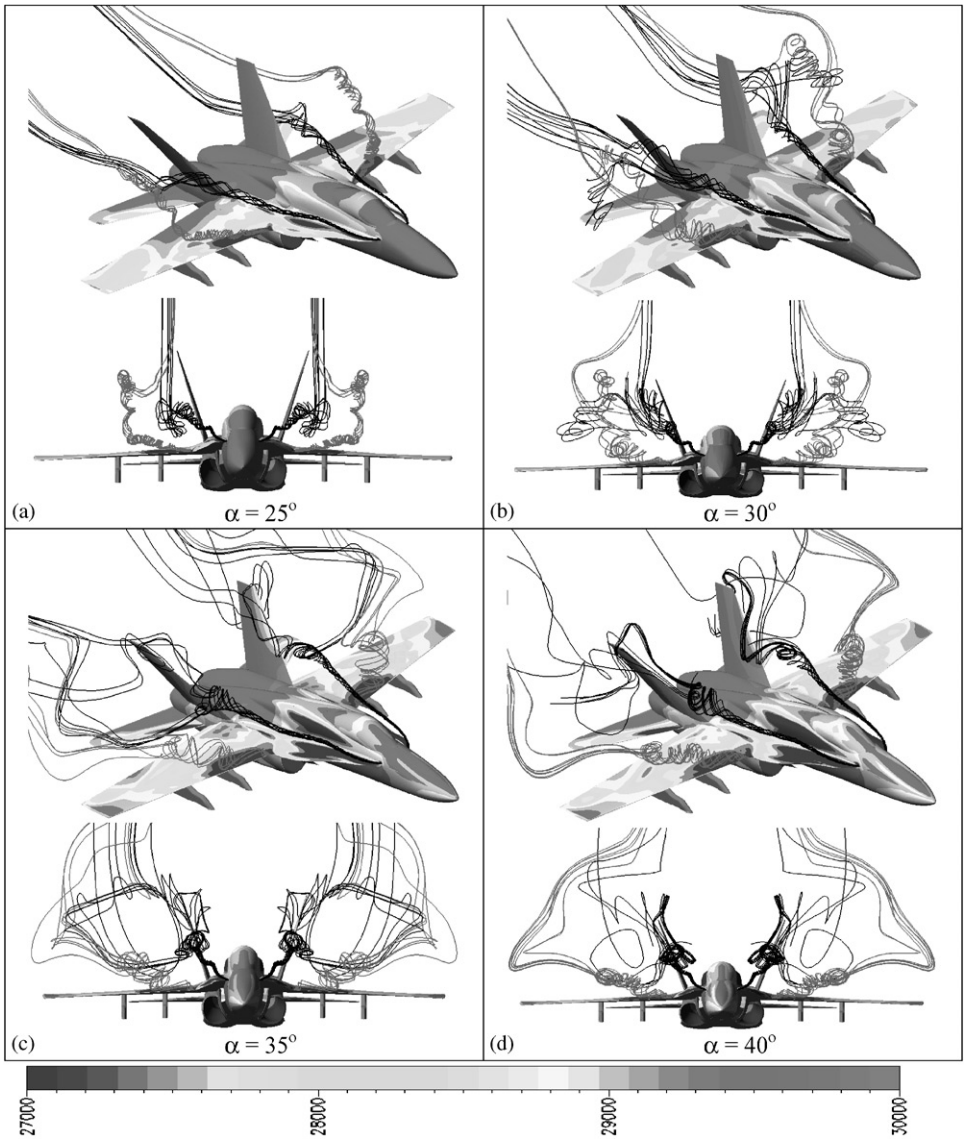

Fig. 6. Three-dimensional and front view snapshots of the F/A-18 aircraft showing the instantaneous streamlines of the LEX and the wing leading edge.

vortex core started to disappear due to vortex diffusion. The vortex core is no longer visible at $\alpha = 40^{\circ}$, which shows that the onset of vortex breakdown moved upstream of the leading edge of the wing root. The total pressure contours on cross-flow plane at the leading edge of the vertical tail root ($x = 11$ m) are shown in Fig. 8. The core of the LEX vortex can only be seen at $\alpha = 25^{\circ}$. The core of the LEX vortex disappears at higher angles of attack due to the upstream motion of the vortex breakdown flow. The core of the LEX and wing vortices can be seen outboard of the vertical tail at all angles of attack.

4.2. *Unsteady aeroelastic loads on the vertical tail*

In order to analyze the unsteady pressure and differential pressure across the tail, the unsteady pressure is monitored on both sides of the vertical tail at 16 selected locations. The locations of the points are selected to match most of the locations of previous experimental and flight-test data, see Meyn et al. (1994). Contour plots of the negative pressure

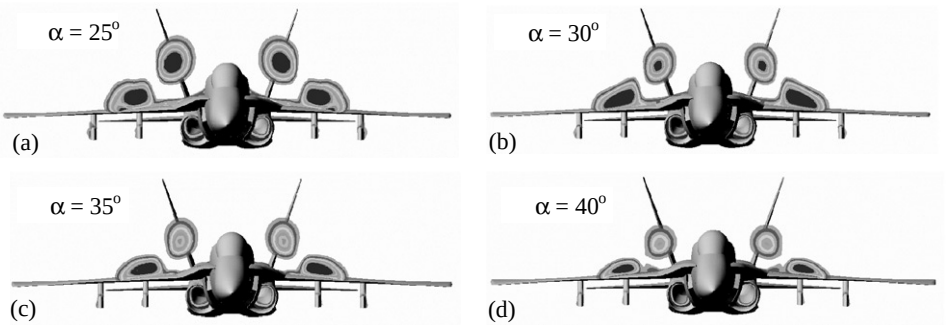

Fig. 7. Total pressure contours on cross-flow plane at the leading edge of the wing root.

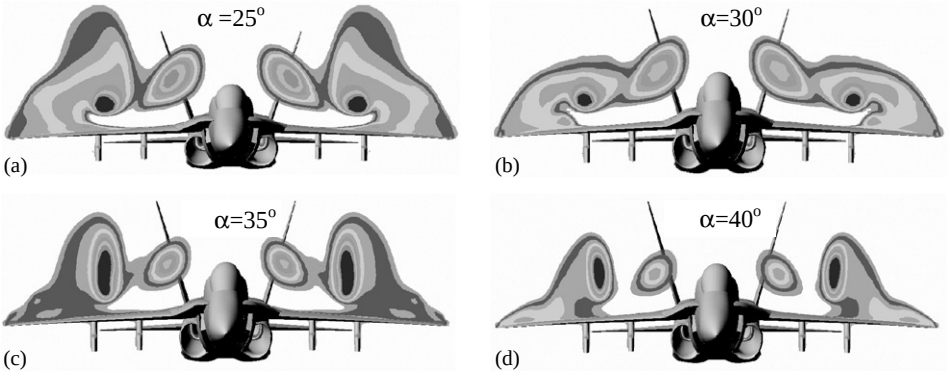

Fig. 8. Total pressure contours on cross-flow plane at the leading edge of the tail root.

coefficient ($-C_p$) on the inboard and outboard surfaces of the vertical tail at $\alpha = 30^\circ$ after 0.1 s are shown in Fig. 9. The contour plots at the tail tip indicate that the net force is directed inboard. While at the tail root and midspan area, the net force is directed outboard. When the differential pressure at the leading edge of the tail is compared to the differential pressure at the trailing edge, the results indicate that the vertical tail is also subject to torsional loads. This is also supported by the chordwise variation of the surface pressure that could generate torsional moments which would excite the natural torsional mode of the tail structure. The torsional loads at the tail tip are directed in the counter-clockwise (CCW) direction, looking to the right tail from top. At the tail root, the torsional loads are directed into the opposite direction. This shows that the vertical tail is subject to both bending and torsional loads.

The differential pressure on the vertical tail is integrated to yield the rbm. The rbm is computed using the differential pressure from the 16 transducer locations on the vertical tail, similarly to what was done in the experimental and flight-test data of Pettit et al. (1994), Meyn et al. (1994) and James and Meyn (1994). The surface pressure surrounding the pressure transducer was assumed to be constant. The loads were assumed to act on the centroid of each area surrounding the transducers. The moment arm is measured from each cell centroid to the tail root. The time histories of the tail rbm coefficient, C_{rbm}, at different angles of attack are shown in Fig. 10. The figure shows unsteady, large-amplitude oscillatory loads at all angles of attack. The amplitude and the mean value of the rbm are maximum in the range 30–40° angles of attack. This is when the vortex breakdown moves upstream of the vertical tail. The history of rbm at lower angles of attack (not shown) did not show this large amplitude of the unsteady loads. Therefore, the vortex breakdown phenomenon appears as the most dominant source of vertical tail buffeting of fighter aircraft. A positive rbm indicates moment that is directed outboard. Therefore, at an angle of attack of 25°, the rbm is mainly directed inboard. At higher angles of attack the rbm is directed outboard.

The root mean square (r.m.s.) of tail rbm coefficient is shown in Fig. 11. The results are compared with the full-scale wind-tunnel data of Pettit et al. (1994) and James and Meyn (1994). The experimental data were obtained using different sensor densities and slightly different model setup. Pettit et al. (1994) used a 6×6 transducer array, while

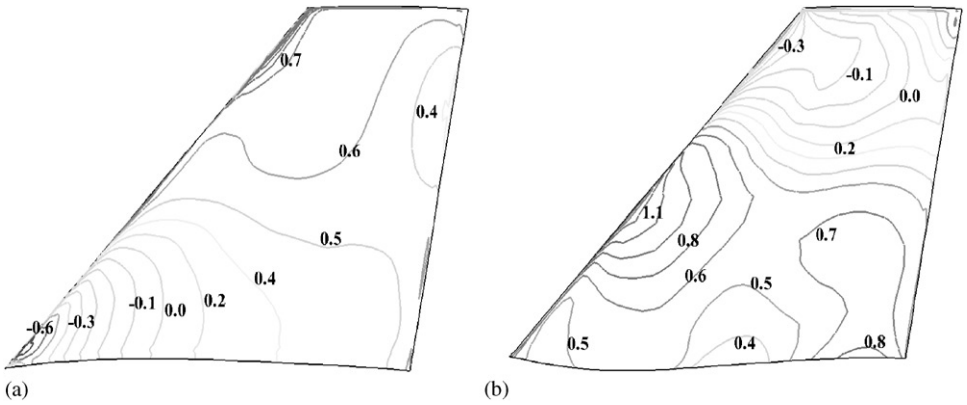

Fig. 9. Contour lines of pressure coefficient, $-C_p$, over the surfaces of the vertical tail. (a) Inboard surface; (b) outboard surface.

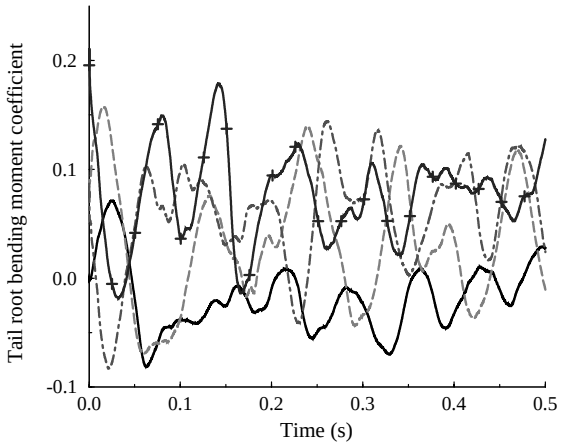

Fig. 10. The time history of the tail rbm coefficient: ——, $\alpha = 25°$;– – –, $\alpha = 30°$; – - –, $\alpha = 35°$; + — +, $\alpha = 40°$.

James and Meyn (1994) used a 6×8 transducer array. James and Meyn (1994) showed that the density of the transducer array affects the integration of the buffet loads on the vertical tail. The results compare well with the experimental data over wide range of angles of attack. The maximum rbm occurs around the 30° angle of attack. That is when the vortex breakdown is completely ahead of the leading edge of the vertical tail. At higher angles of attack, the rbm decreases due to the diffusion of the vortex breakdown flow before it impinges upon the vertical tail. At low angles of attack ($\alpha < 25°$), there is still substantial amount of buffet. This buffet occurs even when the onset of vortex breakdown is downstream of the vertical tail. This observation suggests that the vortex breakdown may not be the only source of vertical tail buffeting of fighter aircraft. This was also observed experimentally by Gursul and Xie (1999). Several unsteady phenomena may contribute to the tail buffeting at lower angles of attack, such as vortex shedding, wakes from different parts of the aircraft, unsteady flow separation from the leading edge of the vertical tail (as observed in Fig. 4), and adverse feedback form the unsteady location of the onset of vortex breakdown.

4.3. Unsteady pressure at 45% chord and 60% span

Several publications have reported experimental and flight-test data at the 45% chord and 60% span point on the vertical tail. Thus, the unsteady pressure history at this point was monitored and analyzed for comparison. This would insure that results from different sources of tests and flight data have a common point for comparison. The time histories of the inboard, outboard, and differential unsteady pressure coefficients at the 45% chord and 60% span point are shown in Fig. 12. The figure indicates that the inboard surface of the tail experienced larger amplitude of fluctuation

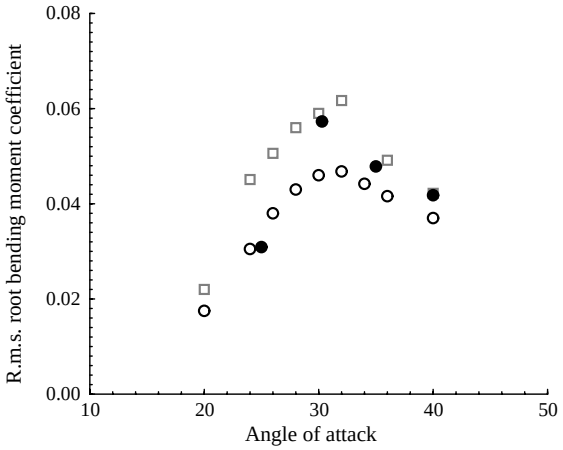

Fig. 11. RMS of tail rbm coefficient: ○, full-scale model (James and Meyn, 1994); □, full-scale model (Pettit et al., 1994); ●, present computation.

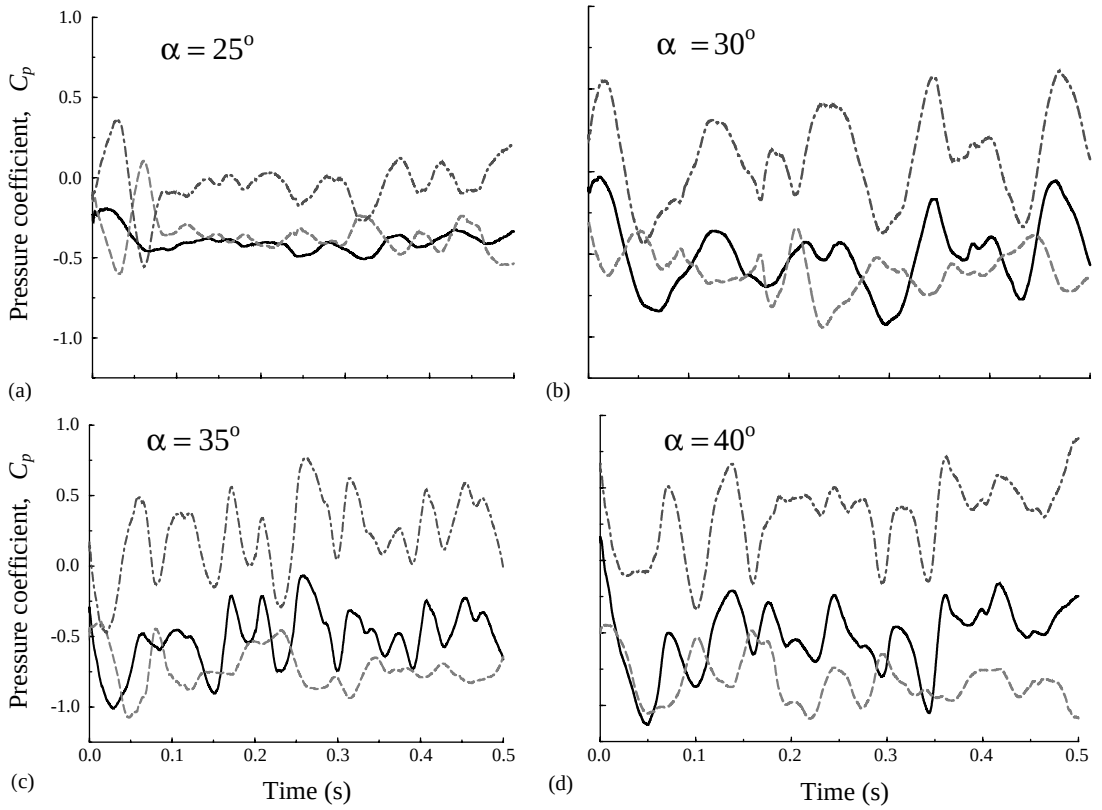

Fig. 12. The time histories of pressure coefficients on the vertical tail at 45% chord, 60% span: ——, inboard pressure; – – –, outboard pressure; – – –, differential pressure.

than the outboard surface, except at 25° angle of attack. This indicates that the inboard surface of the vertical tail has a more significant contribution in the unsteadiness of the problem than the outboard surface.

The r.m.s. of inboard, outboard and differential pressure coefficients are shown in Fig. 13. The results are compared with flight-test data, full-scale and 16%-scale wind-tunnel data of Meyn et al. (1994). The results compare well with the

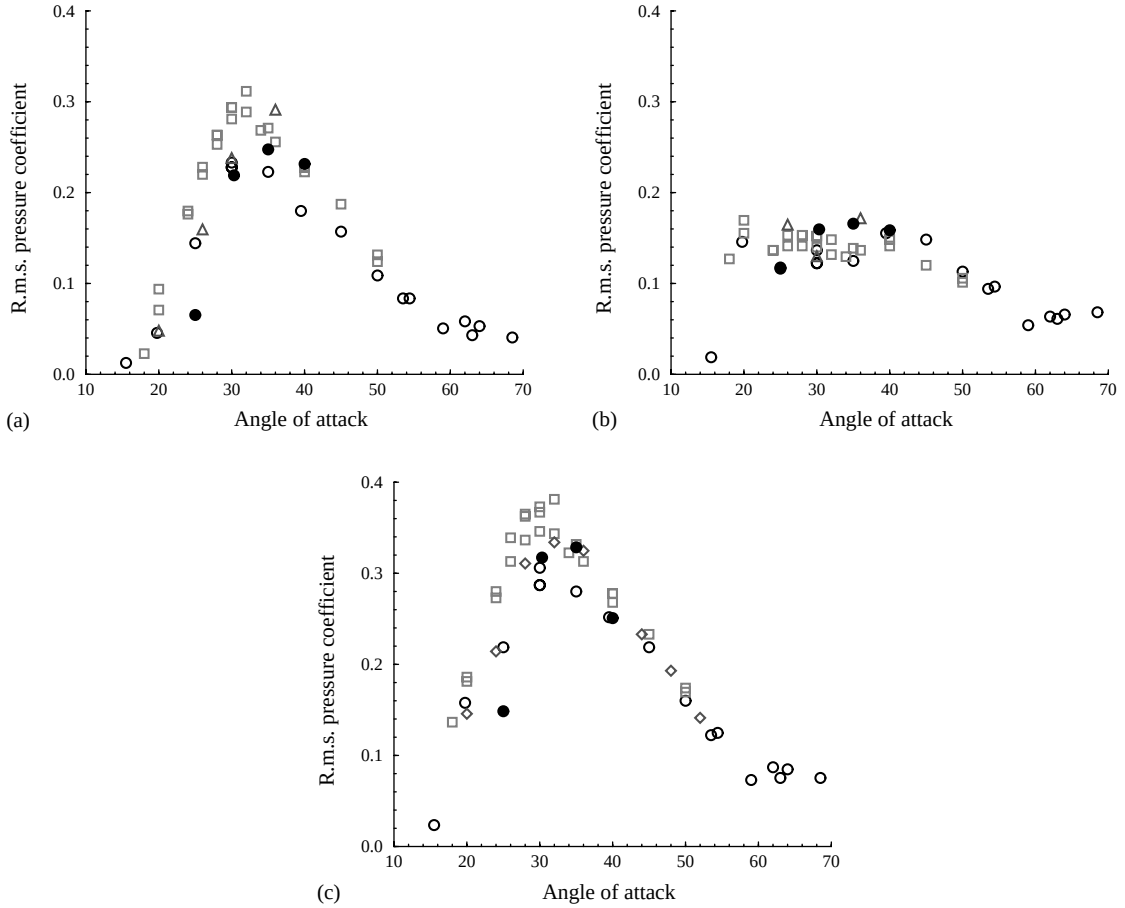

Fig. 13. RMS pressure coefficient at 45% chord and 60% span point: (a) inboard pressure; (b) outboard pressure; (c) differential pressure. ○, flight data (Meyn et al. 1994); □, full-scale model (Meyn et al., 1994); △, 16% scale model (Meyn et al. 1994); ●, present computation.

experimental and flight-test data over wide range of angles of attack. The r.m.s. pressure of the inboard surface is larger than the r.m.s. pressure of the outboard surface, which emphasizes the previous conclusion that the inboard surface of the vertical tail has more significant contribution in the unsteadiness of the buffet problem. In addition, the results indicate that the r.m.s. of the outboard pressure is less sensitive to the angle of attack than the inboard pressure. This is probably because of the location of the vortical flow with respect to the tail. Initially, most of the vortical flow exists at the outer surface of the tail. As the angle of attack increases, the vortex breakdown flow moves inboard, imposing different levels of unsteady pressure on the inboard surface of the tail. Analysis of the differential pressure at the 16 transducer locations revealed that the leading edge of the vertical tail experiences the largest r.m.s. pressures, while the trailing edge of the vertical tail experiences the lowest r.m.s. pressures. The r.m.s. of the differential pressure at the root of the vertical tail is larger than the r.m.s. differential pressure at the tail tip. This observation applies to all angles of attack considered.

Power spectral density (PSD) of the history of the unsteady pressure coefficients was computed using MATLAB® toolbox. The buffet pressure spectra is normalized by the freestream dynamic pressure and it is presented as $\sqrt{nF(n)}$, where $F(n)$ is the buffet excitation PSD and n is the nondimensional frequency. The PSD is computed based on a time span of 0.5 s. The length of the time record is fairly sufficient since there are no abrupt changes in the signal and the vertical tail response is nearly periodic, see the next section. The predominant frequencies of the buffet pressure peaks are shown in Fig. 14 for the inboard pressure, outboard pressure, and differential pressure coefficients. The pressure frequencies compared quite well with the experimental and flight-test data over the angle of attack range. In general, the peaks of the buffet excitation shift into lower frequencies as the angle of attack increases. The frequency shift at high

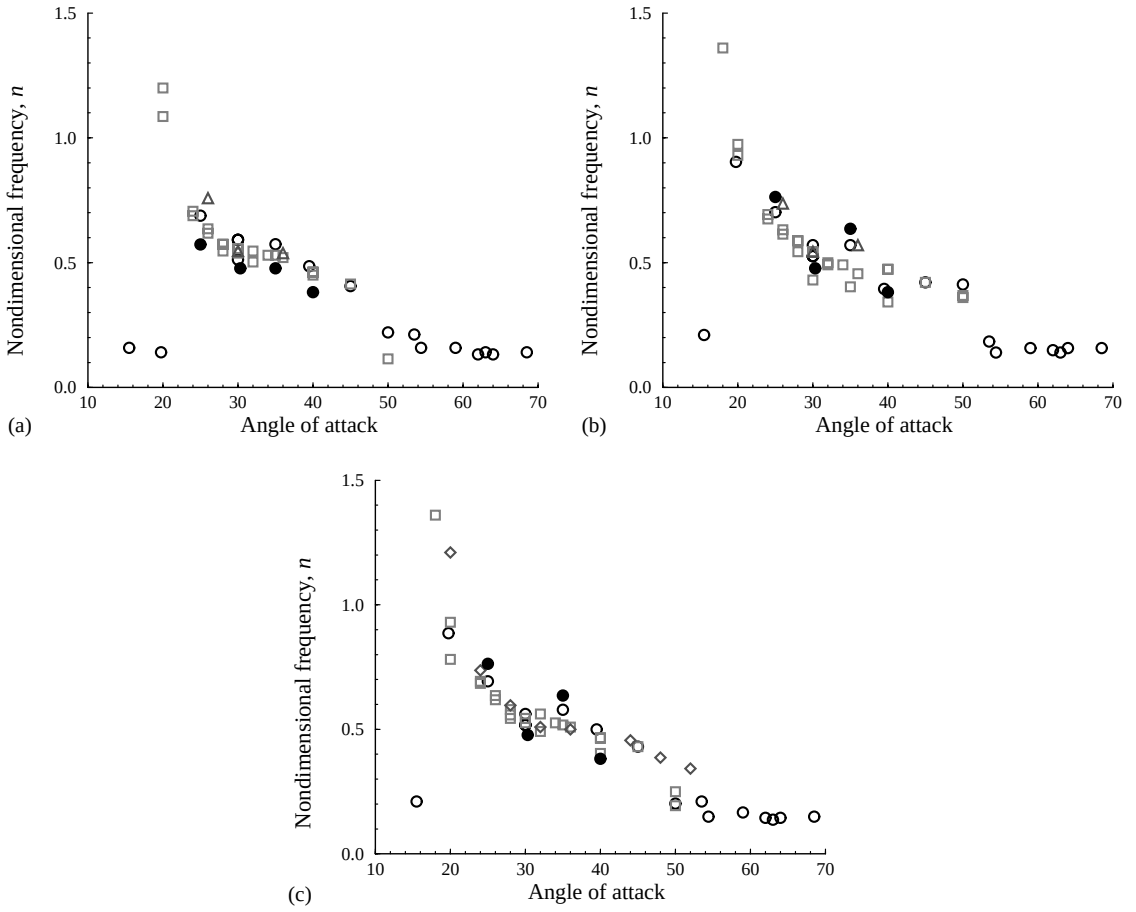

Fig. 14. Predominant frequency of buffet pressure peaks at 45% chord and 60% span point: (a) inboard pressure; (b) outboard pressure; (c) differential pressure. ○, flight data (Meyn et al. 1994); □, full-scale model (Meyn et al., 1994); △, 16% scale model (Meyn et al., 1994); ●, present computation.

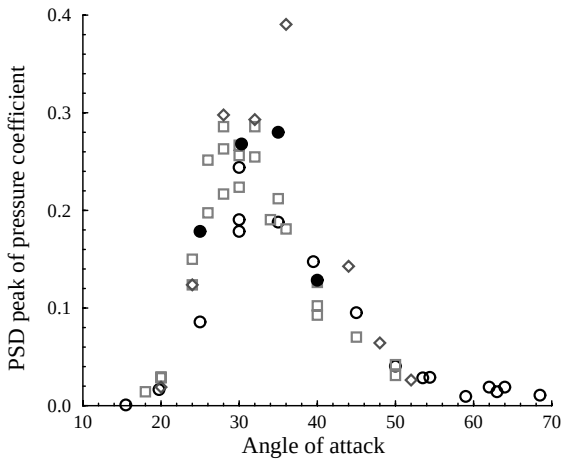

Fig. 15. PSD peak of differential pressure coefficient at 45% chord and 60% span point: ○, flight data (Meyn et al., 1994); □, full-scale model (Meyn et al., 1994); ◇, 12% scale model (Meyn et al., 1994); ●, present computation.

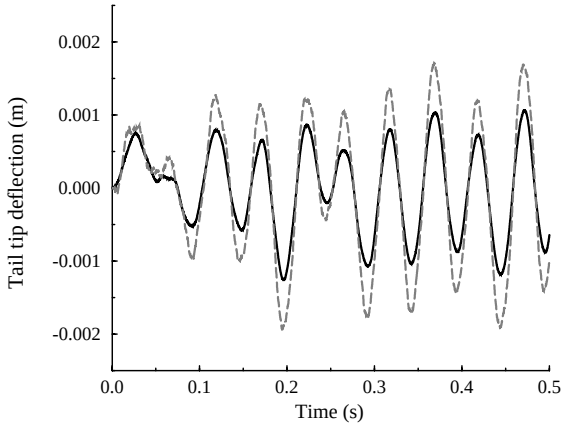

Fig. 16. The time histories of the normal deflection of the tail tip of the vertical tail: ——, leading edge;– – –, trailing edge.

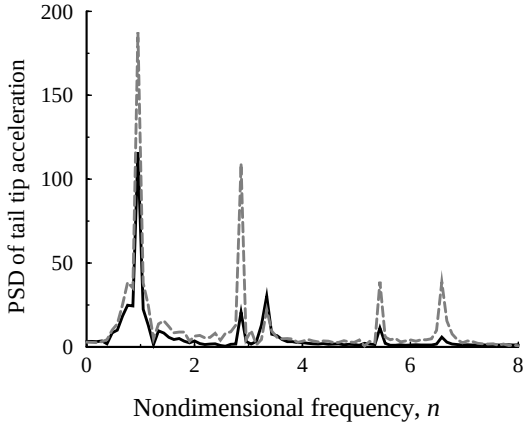

Fig. 17. PSD of tail tip acceleration: ——, leading edge;– – –, trailing edge.

angles of attack has been observed by several researchers using different models, e.g., Washburn et al. (1993), Pettit et al. (1994), and Meyn et al. (1994).

The PSD peak of the excitation spectra of the differential pressure coefficient is compared with the experimental data in Fig. 15. The peak power of the differential pressure compares quite well with the experimental data over the angle of attack range. The maximum buffet excitation occurs in the 30–35° range of angles of attack. A large increase in the peak of the buffet differential pressure occurs at 25° angle of attack; an indication that the vortex breakdown flow moved ahead of the leading edge of the vertical tail.

4.4. Aeroelastic deformation

The time histories of the tail tip normal deflections are shown in Fig. 16 for the case of an angle of attack of 30°. The figure shows the oscillatory nature of the deflection around a slightly negative mean toward the outboard direction. This is because most of the vortical flow exists at the outboard of the vortical tails as shown in Figs. 6–8. The vortical flow produces suction pressures, which tends to move the tail surface toward the outboard direction. The trailing edge of the tail experiences higher amplitude of deflections than that of the leading edge. This indicates that the vertical tail exhibits torsional response, in addition to the primary bending response. This observation is consistent with the torsional loads observed upon the vertical tail. The PSD of the tail tip acceleration is shown in Fig. 17 for the leading- and trailing-edge points. The figure shows that the acceleration power at the trailing-edge point is larger than that at the leading-edge point. The predominant nondimensional frequency of the tail tip acceleration is 1.0, in agreement with the experimental value reported by Pettit et al. (1994). The first two peaks occur around the nondimensional frequencies of 1 and 3,

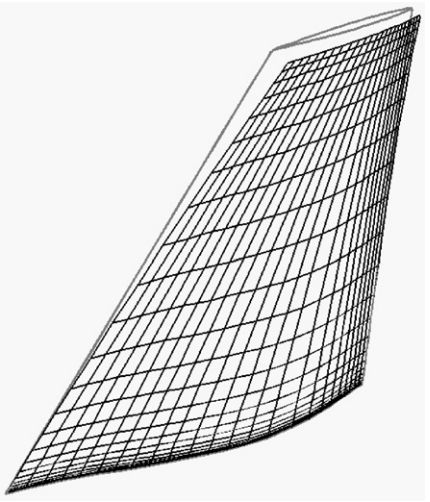

Fig. 18. The deformed shape of the vertical tail after 0.11 s.

corresponding to the first bending and torsion modes. The first peak is significantly higher than the second peak, which indicates the dominance of the first bending mode. A third peak occurs at the second bending mode but with smaller level than the peaks at the first two modes, which indicates that the contribution of the second bending mode is not significant at these conditions.

A snapshot of the deformed vertical tail of the F/A-18 aircraft after 0.11 s is shown in Fig. 18. This snapshot is corresponding to the point of maximum deflection in the third cycle of response. In this figure, the deformation is magnified four times for the sake of clarity. As shown in the figure, the vertical tail responds mainly in the first bending mode. The tail also exhibits torsional deflections in the CCW direction looking upstream.

5. Concluding remarks

A time-accurate multidisciplinary analysis of vertical tail buffeting of F/A-18 aircraft is conducted at typical flight conditions to identify the characteristics of tail buffeting of fighter aircraft. The flow field results indicated that the most dominant source of vertical tail buffeting is the vortex breakdown. However, a substantial amount of buffeting is observed at low angles of attack where the vortex breakdown occurs downstream of the vertical tail. This indicated buffet contributions from other sources, such as vortex shedding, unsteady flow separation from the leading edge of the vertical tail, wakes from other parts of the aircraft, and adverse feedback from the unsteadiness of the location of the vortex breakdown. The investigation revealed that the inboard surface of the vertical tail has a more significant contribution in the unsteadiness of the buffet problem than the outboard surface. The outboard surface pressure of the vertical tail is also less sensitive to the angle of attack than the pressure on the inboard surface. The buffet excitation peaks shift to lower frequencies as the angle of attack increases. The vertical tail of the F/A-18 aircraft responded mainly in the first bending and torsional modes. The vertical tail oscillates towards the outboard direction, due to outboard suction of the primary leading-edge vortex. The computational results are compared to and are found to be in close agreement with flight and experimental data over the considered range of angles of attack.

Acknowledgements

This research work is supported by the AFRL/VA directorate of the United States Air Force. The authors wish to acknowledge Don Kinsey of Wright-Patterson Air Force base for his support of the MDICE-aerostructures environment. Vincent Harrand, Viji Parthasarathy, Mark Underwood, and Stacey Rock of CFDRC provided invaluable support during this study.

References

Bean, D.E., Lee, B.H.K., 1994. Correlation of wind tunnel and flight test data for F/A-18 vertical tail buffet. AIAA Paper 94-1400.

Brown, S.A., 1997 Displacement extrapolation for CFD and CSM analysis. AIAA Paper 97-1090.

Cole, S.R., Moss, S.W., Dogget Jr., R.V., 1990. Some buffet response characteristics of a twin-vertical-tail configuration. NASA TM-102749.

Fisher, D.F., Del Frate, J.H., Richwine, D., 1990. In-flight flow visualization characteristics of the NASA F-18 high alpha research vehicle at high angles of attack. NASA TM 4193.

Gee, K., Murman, S., Schiff, L., 1995. Computational analysis of F/A-18 tail buffet. AIAA Paper 95-3440.

Gursul, I., Xie, W., 1999. Buffeting flows over delta wings. AIAA Journal 37, 58–65.

Hall, L.H., 1999. Navier–Stokes/6-DOF analysis of the JDAM store separation from the F/A-18C aircraft. AIAA Paper 99-0121.

James, K.D., Meyn, L.A., 1994. Dependence of integrated vertical-tail buffet loads for F/A-18 on sensor density. SAE Paper 941140.

Jumper, E.J., Nelson, R.C., Cheung, K., 1993. A simple criterion for vortex breakdown. AIAA Paper 93-0866.

Kandil, O.A., Massey, S.J., Sheta, F., 1996. Aerostructural vortical flow interactions with applications to F/A-18 and F-117 tail buffet. NASA-CR-203245, also in NASA/CP-1998-207676, 1375–1388.

Kandil, O.A., Sheta, E.F., Massey, S.J., 1997. Fluid/structure twin tail buffet response over a wide range of angles of attack. AIAA Paper 97-2261.

Kingsley, G.M., Siegel, J.M., Harrand, V.J., Lawrence, C., Luker, J., 1998. Development of the multi-disciplinary computing environment (MDICE). AIAA Paper 98-4738.

Lee, B., Brown, D., 1990. Wind tunnel studies of F/A-18 tail buffet. AIAA Paper 90-1432.

Lee, B., Valerio, N., 1994. Vortical flow structure near the F/A-18 LEX at high incidence. Journal of Aircraft 31, 1221–1223.

Lee, B., Brown, D., Zgela, M., Poirel, D., 1990. Wind tunnel investigation and flight tests of tail buffet on the CF-18 aircraft. AGARD CP No. 483.

Meyn, L.A., James, K.D., 1993. Full scale wind tunnel studies of F/A-18 tail buffet. AIAA Paper 93-3519.

Meyn, L.A., James, K.D., Green, R.J., 1994. Correlation of F/A-18 tail buffet results. High Alpha Projects and Technology Conference, Dryden Flight Research Center, Edwards, CA, USA. July 1994.

Moses, R.W., 1997 Vertical tail buffeting alleviation using piezoelectric actuators—some results of the actively controlled response of buffet-affected tails (ACROBAT) program. NASA TM 110336.

Moses, R.W., Huttsell, L.J., 2000. Fin buffeting features of an early F-22 model. AIAA Paper 2000-1695.

Moses, R.W., Pendleton, E., 1996 A comparison of pressure measurements between a full-scale and a 1/6-Scale F/A-18 twin tail during buffet. NASA-TM-110282.

Pettit, C., Brown, D., Pendleton, E., 1994. Wind tunnel tests of full-scale F/A-18 twin Tail buffet: A summary of pressure and response measurements. AIAA Paper 94-3476.

Rizk, Y., Guruswamy, G., Gee, K., 1992a. Numerical investigation of tail buffet on F-18 aircraft. AIAA Paper 92-2673.

Rizk, Y., Guruswamy, G., Gee, K., 1992b. Computational study of F-18 vortex induced tail buffet. AIAA Paper 92-4699.

Sellers III, W.L., Meyers, J.F., Hepner, T.E., 1988. LDV survey over a fighter model at moderate to high angle of attack. SAE Paper 88-1448.

Shah, G.H., 1991. Wind-tunnel investigation of aerodynamic and tail buffet characteristics of leading-edge extension modifications to the F/A-18. AIAA Paper 91-2889.

Sheta, E.F., 2000. Effect of stream-wise fences on twin-tail buffet responses. AIAA Paper 2000-4410.

Sheta, E.F., Kandil, O.A., 1998. Effect of configuration pitching motion on twin-tail buffet response. AIAA Paper 98-0520.

Sheta, E.F., Kandil, O.A., 1999. Effect of dynamic rolling oscillations on twin-tail buffet response. AIAA Paper 99-0792.

Sheta, E.F., Stacey, S.G., Huttsell, L.J., 2001. Characteristics of vertical tail buffet of F/A-18 aircraft. AIAA Paper 2001-0710.

Washburn, A.E., Jenkins, L.N., Ferman, M.A., 1993 Experimental investigation of vortex-fin interaction. AIAA Paper 93-0050.

Wentz, W.H., 1987. Vortex-fin interaction on a fighter aircraft. AIAA Paper 87-2474.

Yang, H.Q., Wang, Z.J., 1994. Interaction of shock wave with a flexible structure. AIAA Paper 94-0362.